Rayleigh instability of the inverted one-cell amphibian embryo

Comron Nouri[1,2]**, Roel Luppes**[3]**, Arthur E P Veldman**[3]**, Jack A Tuszynski**[2]
and Richard Gordon[1,4]

[1] Department of Radiology, University of Manitoba, Winnipeg, Canada
[2] Department of Physics, University of Alberta, Edmonton Alberta, Canada
[3] Institute of Mathematics & Computing Science, University of Groningen, Groningen,
The Netherlands
[4] Departments of Computer Science and Electrical & Computer Engineering,
University of Manitoba, Winnipeg, Canada

E-mail: nouri@ualberta.ca, jtus@phys.ualberta.ca, R.Luppes@math.rug.nl,
A.E.P.Veldman@math.rug.nl, gordonr@cc.umanitoba.ca

Abstract
The one-cell amphibian embryo is modeled as a rigid spherical shell containing equal volumes
of two immiscible fluids with different densities and viscosities and a surface tension between
them. The fluids represent denser yolk in the bottom hemisphere and clearer cytoplasm and
the germinal vesicle in the top hemisphere. The unstable equilibrium configuration of the
inverted system (the heavier fluid on top) depends on the value of the contact angle. The
theoretically calculated normal modes of perturbation and the instability of each mode are in
agreement with the results from ComFlo computational fluid dynamic simulations of the same
system. The two dominant types of modes of perturbation give rise to axisymmetric and
asymmetric sloshing of the cytoplasm of the inverted embryos, respectively. This work
quantifies our hypothesis that the axisymmetric mode corresponds to failure of development,
and the asymmetric sloshing mode corresponds to development proceeding normally, but with
reversed pigmentation, for inverted embryos.

Nomenclature

a	radius of the sphere or the spherical embryo
ρ_1	density of the heavier liquid
ρ_2	density of the lighter liquid
ρ	density contrast between the two liquids
σ	interfacial tension between the two liquids
x, y, z	Cartesian coordinates
r, θ, z	polar coordinates
p_σ, p_g	pressures due to surface tension and gravity
θ_0	contact angle
C	speed of wave on a membrane or interface of liquids
U	displacement of the surface from equilibrium
X, Y, T	r, θ, and time-dependent portions of function u
J_m, Y_m	Bessel functions of the first and second kind
i	$\sqrt{-1}$
q_{mn}	the nth zero of J'_m
f_{mn}	the functional form of the mode characterized by (m, n)
ω_{mn}	frequency of oscillation of the mode f_{mn}
B_{mn}	the normalization factor of f_{mn}
ε	initial amplitude of small perturbations
$S(m, n, \varepsilon)$	surface area of the interface disturbed by f_{mn} with amplitude ε
$\Delta U^g_{mn}, \Delta U^\sigma_{mn}$	changes in the gravitational potential energy and surface energy of the perturbed system
s_{mn}, u_{mn}	dimensionless values related to the surface and gravitational potential energies of the modes of perturbation defined in the text
α	growth rate of modes of perturbation
τ	period of oscillation of the modes in the upright system

γ	growth rate of the hanging part of a chain on a table
L	total length of the chain
$m_{\text{eff}}, m_{\text{eff 11}}$	the effective mass involved in oscillation and that for mode 11

Introduction

Amphibian eggs are bottom heavy, with more of the dense yolk platelets in the bottom hemisphere than the top. When tipped, they rapidly right themselves (Gordon *et al* 2006). This is easy to observe in those eggs that are dark on top and lightly pigmented at the bottom, such as the fertilized axolotl egg (*Ambystoma mexicanum*), which we can think of as a one-cell amphibian embryo (Bordzilovskaya *et al* 1989). When such a one-cell amphibian embryo is inverted prior to the first cell division, it either develops with pigmentation of dorsal and ventral skin reversed, or it does not develop at all past gastrulation (Chung and Malacinski 1982, 1983, Malacinski and Neff 1989, Neff and Malacinski 1982, Neff *et al* 1986, 1984, 1990, Wakahara *et al* 1984, 1985). In microgravity, where up and down do not matter, 'although early embryonic stages showed some abnormalities, the embryos were able to . . . produce nearly normal larvae' (Black *et al* 1996). There is abundant experimental evidence that links the alignment of cortical microtubules (those just below the cell membrane) with the spontaneous cortical rotation that happens before the first cell division (Elinson and Rowning 1988, Gerhart *et al* 1989). This cortical rotation is known to correlate precisely with the later developing dorsal–ventral axis and left/right bilateral symmetry of the embryo (Chang *et al* 1999, Elinson and Holowacz 1995, Gerhart *et al* 1989). Some experiments also show that forced cortical rotation, that is, rotating the cortex using an external apparatus, works as well in dorsal–ventral axis determination (Ancel and Vintemberger 1948, Denegre and Danilchik 1993, Kirschner *et al* 1980, Phillips *et al* 1996). This remarkable observation suggests that something purely physical and macroscopic is involved in this stage of development. Therefore we hypothesized that the way the denser yolk flows down to the bottom of the inverted embryo is the critical factor for inverted one-cell embryos: axisymmetric flow terminates development, while asymmetric sloshing permits normal development (Flint *et al* 1989). In the present study we attempt to understand the probability of each type of flow using a simplified two-liquid model. In this model we consider a sphere filled with two immiscible liquids with equal volume and different densities, modeling the heavier yolk and less dense cytoplasm inside the egg, with the heavier liquid on top to represent inversion of the one-cell amphibian embryo.

We divide the problem into two separate steps. First we calculate the unstable equilibrium configuration of the system when the heavier liquid is on top, and try to find the equation describing the non-planar interfacial surface between the two liquids. This, amongst other things, depends on the relative densities and the interfacial tension between the two liquids, the radius of the sphere and the contact angle of the interfacial surface with the surface of the sphere where they
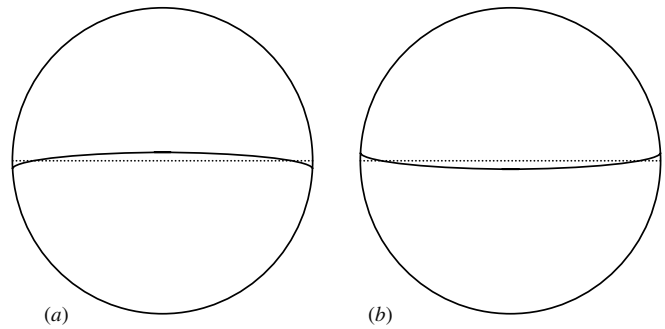

(*a*)   (*b*)

Figure 1. Schematic diagram of the unstable equilibrium of a sphere filled equally with two immiscible liquids with the heavy one on top, (*a*) when the contact angle is less than $90°$ and (*b*) when it is more than $90°$. The dotted line shows the flat surface when the contact angle $= 90°$.

touch. The contact angle, in turn, depends on the type of materials comprising the liquids and that of the sphere (Kane and Sternheim 1983) (figure 1).

Next, we introduce some small deviation from the equilibrium configuration and study the growth rate of each normal mode of perturbation. This is a Rayleigh-type analysis after Lord Rayleigh's instability analysis of a long cylindrical liquid (Gordon *et al* 1972, 1975, Rayleigh 1879a, 1879b, 1892, 1964). This will show the likelihood of any type of flow of the heavier liquid down toward a stable configuration in which it finally settles at the bottom.

The outcome of the analytical (mathematical) model is compared with results obtained with the simulation tool ComFlo (Gerrits and Veldman 2003, Kleefsman *et al* 2005, Luppes *et al* 2005, 2006, Veldman *et al* 2007). Based on the Navier–Stokes equations for free-surface flows, this computational fluid dynamics (CFD) program can simulate the sloshing of two immiscible fluids with different densities and viscosities by means of finite-volume discretization techniques, including specially designed free-surface tracking algorithms.

Unstable equilibrium configuration

Suppose we have a sphere filled with two immiscible liquids with different densities and equal volumes so that each one fills half of the volume of the sphere. In the equilibrium state, the heavy liquid (the one with higher density) is at the bottom half of the sphere and the lighter one on top. The interfacial surface between them in general is not a flat surface and its shape depends on the contact angle between the interfacial surface and the inner wall of the sphere and also depends on the surface tension and gravity. Its meniscus shape is similar to that of water in a partially filled glass of water or a test tube. It has a curvature and its shape is axisymmetric when the container's cross-section is circular. In Cartesian coordinates the equation of the surface can be described as $z(x, y)$. In cylindrical coordinates, however, it takes a simpler form of $z(r)$, independent of θ because of its azimuthal symmetry. When the heavy liquid is on top, there is also an equilibrium state which is, however, unstable, but the general form of the interface is almost the same.

In general, we have two fluids with different densities ρ_1 and ρ_2 (with $\rho_1 > \rho_2$). The important parameter influencing the behavior of the system is the density contrast $\rho = \rho_1 - \rho_2$. It is fairly straightforward, by balancing the pressures due to surface tension of the curved surface with that due to gravity, to write down the differential equation governing the shape of the interfacial surface and solve for its azimuthally symmetric equation, $z(r)$ (Rowlinson and Widom 1982). The solution in the cases when the contact angle is sufficiently close to $90°$ is

$$z(r) = A J_0(i\beta r), \tag{1}$$

where the real constant A is defined by

$$A = \frac{-\cot\theta_0}{i\beta J_1(i\beta a)}, \tag{2}$$

arising from the boundary condition that the contact angle at $r = a$ (where a is the radius of the sphere or the embryo) should be θ_0. The function $J_m(x)$ is the mth-order Bessel function of the first kind (Greenberg 1998). σ is the surface tension, i is the imaginary unit number and $\beta = \sqrt{\rho g/\sigma}$. As an example, $\beta = 370\ \mathrm{m}^{-1}$ for water at $20\,°C$, with $\sigma = 7.3 \times 10^{-2}\ \mathrm{N\ m}^{-1}$, $\rho = 10^3\ \mathrm{kg\ m}^{-3}$ and $g = 9.8\ \mathrm{kg\ m\ s}^{-2}$. This is the reason why the capillary effects become significant for systems with dimensions of a few millimeters or smaller, i.e., at the capillary length (de Gennes *et al* 2004). Equation (1) gives the unstable equilibrium configuration of the surface of the fluid when it is occupying the upper half of the sphere. In the following we attempt to find the normal modes of perturbation and the functional form of growth of the normal modes of this surface. While the above surface seems to be complicated for the upcoming analysis, we note that for the case of $\theta_0 = \pi/2$ we have $A = 0$ and the surface will be a flat plane. Therefore, for simplicity we take the contact angle to be at this value for the rest of the calculations, i.e., we assume a flat plane as the separation surface at equilibrium.

Normal modes of vibrations of the fluid surface

The instability of different modes of perturbation can be estimated by the increase in the surface area of the fluid and also by the imbalance it creates in the forces that tend to move the system away from the unstable equilibrium.

The modes of perturbation are the vibration modes of the surface coming from the solution to the wave equation for the circular, planar interface between the two fluids. We model the circular interface with a vibrating membrane with displacement $u(r, \theta, t)$ and Neumann boundary conditions, since for our case the contact angle is taken as $90°$. Therefore the radial derivative of the displacement should vanish at the boundary ($r = a$). This is not a precise model, but it will be proved that it is a good enough approximation for our purposes here. The wave equation for a membrane is given by

$$c^2 \nabla^2 u = \frac{\partial^2 u}{\partial t^2} \tag{3}$$

where the constant c is the propagation velocity of waves on the membrane. Since the equation is linear, the solution

can be found straightforwardly by separation of variables and applying the boundary conditions (Greenberg 1998):

$$u(r, \theta, t) = J_m\left(\frac{\omega r}{c}\right) e^{\pm im\theta}\, e^{i\omega t} \tag{4}$$

where ω is the frequency of vibration of the mode, m is a nonnegative integer and $J_m(s)$ denotes the Bessel function of the first kind and of order m, and is defined by (Greenberg 1998)

$$J_m(s) = \sum_{k=0}^{\infty} \frac{(-1)^k}{k!(k+m)!} \left(\frac{s}{2}\right)^{2k+m}. \tag{5}$$

The zeros of these functions can be found in many handbooks (Abramowitz and Stegun 1965). For the surface of the fluid, the values of s in $J_m(s)$ should be chosen in such a way that fluid volume be conserved. These values correspond to the zeros of the derivatives of the Bessel functions since $\int s J_m(s)\,ds$ vanishes at zeros of $J_m'(s)$ for the case $m = 0$. For the other cases ($m \neq 0$) the volume under each mode also vanishes due to periodicity of $Y_m(\theta)$. Therefore, we consider the truncating point of each Bessel function $J_m(s)$ at the zeros of $J_m'(s)$. This allows us to have the conservation of fluid volume for our system in all cases, as well as satisfying the condition for the contact angle of $90°$, with which we started these calculations. We denote the nth zero of $J_m'(s)$ by q_{mn}. The numerical values of q_{mn} for the first few Bessel functions are given in table 1.

The boundary condition (conservation of fluid volume, or contact angle of $90°$) requires $q_{mn} = \omega a/c$, which discretizes the frequencies as

$$\omega_{mn} = \frac{q_{mn}c}{a}. \tag{6}$$

These are the frequencies of the corresponding modes of vibration

$$u_{mn}(r, \theta, t) = \cos(\omega_{mn}t + \varphi_t)\cos(m\theta + \varphi_\theta)J_m\left(\frac{\omega_{mn}r}{c}\right) \tag{7}$$

where φ_t and φ_θ denote the corresponding phases, which depend on the initial conditions. The general solution for the vibrating interface between the fluids, i.e. equation (3), is a linear combination of all of these terms. For determination of the most unstable mode in our case, however, we only need to concentrate on the following modes of vibration of the membrane and estimate their relative instability:

$$f_{mn}(r, \theta) = B_{mn}\cos(m\theta)J_m\left(\frac{q_{mn}r}{a}\right) \tag{8}$$

where B_{mn} is the normalization factor. These are the main modes of vibration that occur at the interface. Figure 2 shows a few of these modes for an inverted embryo. In order to normalize the functions we demand the dot product of each mode with itself to be unity.

This gives

$$B_{mn} = \frac{1}{a\sqrt{\pi\lambda_{mn}}} \tag{9}$$

where we define

$$\lambda_{mn} = \frac{1 + \delta_{0m}}{q_{mn}^2} \int_0^{q_{mn}} J_m^2(x)x\,dx. \tag{10}$$

Here δ_{0m} denotes the Kronecker delta which is zero for $m \neq 0$ and is unity for $m = 0$. The numerical values of B_{mn} are given in table 1 for the first few modes.
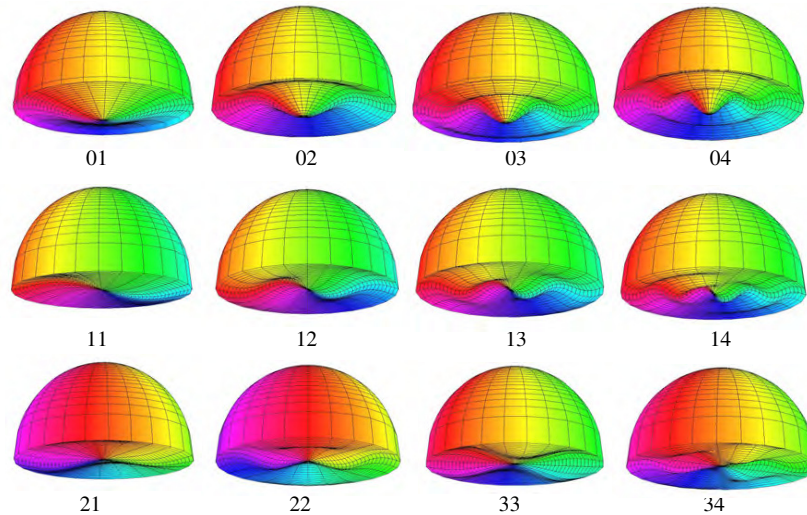
Figure 2. Visualization of different modes of excitation of the interfacial surface when the heavy fluid is on the top half of the sphere. The numbers underneath each mode shows the *m* and *n* parameters for each mode. This figure shows only the heavy fluid on top and is colorful only for visual convenience.

Table 1. This table shows on the columns respectively, mode numbers, the q_{mn} values for each mode, normalization factors in units of $1/a$, values of s_{mn}, the surface energy, u_{mn}, and the gravitational potential energy associated with perturbation with each mode (see the text).

Mode	q_{mn}	B_{mn} $(1/a)$	s_{mn}	ΔU_{mn}^{σ} (nJ)	u_{mn}	ΔU_{mn}^{G} (nJ)
01	3.8317	1.400 81	1.190 82	68.1	0.081 108	−62.0
02	7.0156	1.879 91	2.216 54	127	0.045 035	−34.4
03	10.1735	2.259 42	3.226 73	184	0.031 176	−23.8
04	13.3237	2.583 77	4.232 17	242	0.023 840	−18.2
11	1.8412	1.205 00	0.173 40	9.91	0.059 674	−45.6
12	5.3314	2.346 84	0.980 47	56.1	0.028 897	−22.1
13	8.5363	2.939 69	1.535 74	87.8	0.018 417	−14.1
14	11.7060	3.432 48	2.060 15	118	0.013 508	−10.3
21	3.0542	2.170 02	0.320 16	18.3	0.033 798	−25.8
22	6.7061	2.666 17	1.309 91	74.9	0.022 3895	−17.1
23	9.9695	3.197 10	1.917 74	110	0.015 571	−11.9
24	13.1704	3.654 66	2.469 33	141	0.011 916	−9.11
31	4.2012	2.623 73	0.453 90	26.0	0.023 120	−17.7
32	8.0152	2.955 16	1.606 99	91.9	0.018 225	−13.9
33	11.3460	3.436 63	2.268 95	130	0.013 476	−10.3
34	14.5858	3.864 70	2.850 85	163	0.010 656	−8.15

Estimating the instability of different perturbations

We now consider the instability of a perturbation of the surface of the denser fluid on top from the equilibrium (which is now a flat surface since the contact angle is set at 90°) by one of the above modes in (8) with an amplitude proportional to a small number ε, that is for $B_{mn} = \varepsilon$. The instability of each mode depends on the changes it causes in the total potential energy once the flat interfacial surface is perturbed by that mode with amplitude ε. The total potential energy is composed of two different parts. One is the surface energy due to the surface tension, and the other is the change in the gravitational potential energy of the system. Since the surface tension tends to reduce the area, each mode creates a positive surface energy because the modes increase the surface area once they occur. The increase in surface energy depends on the mode's shape and amplitude. On the other hand, each mode creates some displacement of material away from the equilibrium. This causes a negative gravitational potential

energy for the inverted system. The sum of these two potential energies determines the instability. If the sum of the potential energies is negative, it means that the mode grows and *vice versa*. This sum of potential energies in fact shows whether we go uphill or downhill on the energy landscape when we perturb the interfacial surface from the initially flat state to the shape of the normal mode under consideration.

The surface area can be calculated from

$$S(m, n, \varepsilon) = \int_0^{2\pi} \int_0^a \sqrt{1 + \left(\frac{\partial f_{mn}}{\partial r}\right)^2 + \frac{1}{r^2}\left(\frac{\partial f_{mn}}{\partial \theta}\right)^2} \, r \, dr \, d\theta. \tag{11}$$

Since the amplitude is very small, this can be estimated by expansion of the square root, which gives for the surface area of each mode

$$S(m, n, \varepsilon) = \pi a^2 + \pi s_{mn} \varepsilon^2 + O(\varepsilon^4) \tag{12}$$
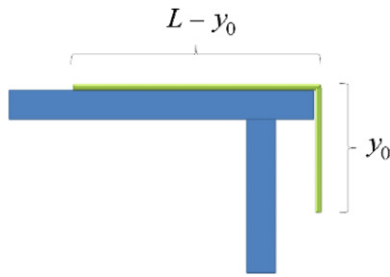
Figure 3. A completely flexible chain of total mass M and length L partly hanging from the edge of a table as a mechanical problem similar to unstable fluid.

where we define

$$s_{mn} = \frac{1 + \delta_{0m}}{2} \int_0^{q_{mn}} J_{m+1}^2(x) x \, dx + \frac{m^2}{2} \int_0^{q_{mn}} \frac{1}{x} J_m^2(x) \, dx. \tag{13}$$

The numerical values of s_{mn} for the first few modes are given in table 1. These values show the percentage of increase in the surface area if we have the interface disturbed by each one of the modes with amplitude $\varepsilon = 0.1a$. The change in surface energy created by each mode is given by

$$\Delta U_{mn}^\sigma = \sigma \, \Delta S(m, n, \varepsilon) = \pi \varepsilon^2 \sigma s_{mn}. \tag{14}$$

As a numerical example with amplitude $\varepsilon = 0.05a$ for a sphere of radius $a = 1$ cm when the two fluids are considered to be water and air this gives $\Delta U_{mn}^\sigma = s_{mn} \times 5.73 \times 10^{-8}$ J. On the other hand, when the interface of the fluid is perturbed by a function $f_{mn}(r, \theta)$ from the flat surface (equilibrium configuration), the total gravitational potential energy for each one of the modes is

$$\Delta U_{mn}^g = -\pi \rho g \varepsilon^2 a^2 u_{mn} \tag{15}$$

where we define the dimensionless number

$$u_{mn} = \frac{1 + \delta_{0m}}{2 q_{mn}^2} \int_0^{q_{mn}} J_m^2(x) x \, dx. \tag{16}$$

The value of the energy is $\Delta U_{mn}^g = -7.64 \times 10^{-7} u_{mn}$ J. The numerical values of u_{mn} and ΔU_{mn} for this example are given in table 1.

Calculation of growth rates of the modes

From an equivalent mechanical problem one can find the functional form of the increase in the amplitude and also the growth rate of each mode of perturbation. In this type of problem, the force acting on the system is proportional to the deviation from equilibrium. Therefore, an equivalent problem can be the following. What is the length of the hanging part as a function of time, of a completely flexible chain of mass M and total length L on a frictionless table with one end hanging down from the edge with length y_0 starting from rest (see figure 3)? From the Newtonian mechanics for this system it is fairly straightforward to derive $y = y_0 \cosh(\gamma t)$, where γ is the growth rate of the hanging part defined by $\gamma = \sqrt{g/L}$. This problem shows that the growth rate depends only on the

gravitational acceleration and the total length of the chain. The important point is that it does not depend on the initial value y_0. On the other hand, the growth rate can be written in terms of the initial potential energy as

$$\gamma = \sqrt{\frac{Mgy_0}{MLy_0}} = \sqrt{\frac{2U_0}{MLy_0}}. \tag{17}$$

To show this for the fluid problem, numerical simulations with ComFlo have been started from one of the modes as the initial surface and repeated for different amplitudes of the initial mode. The results showed that the growth of the amplitude of any normal mode had a hyperbolic cosine form and was independent of the initial amplitude (see figure 4). Therefore, the growth rate of an unstable mode in the inverted one-cell embryo, from analogy with (17) for the equivalent mechanical problem, can be written in terms of the total potential energy of the system in a way that has a dimension of s^{-1}:

$$\alpha = \sqrt{-\frac{\Delta U_{mn}^g + \Delta U_{mn}^\sigma}{\rho \varepsilon^2 a^3}} = \sqrt{\pi \left(-\frac{\sigma}{\rho a^3} s_{mn} + \frac{g}{a} u_{mn} \right)}. \tag{18}$$

If the sum of the two energies is negative $\left| \Delta U_{mn}^g \right| > \left| \Delta U_{mn}^\sigma \right|$, then the mode should grow, and vice versa. For example, for the parameter values we have chosen here, from table 1 we conclude that only modes 01, 11, 21 will grow in this case, and the other modes if created will vanish because they create a positive total change in the potential energy of the system. It might be expected that the modes with the lowest total potential energy grow fastest and vice versa, but this is not quite true because the total mass involved in the dynamics of each mode is different. Making an analytical estimation of this effective mass for each mode is not easy to do. Therefore, we try to estimate it by means of some *in silico* experiments with ComFlo.

Experiments with ComFlo

The outcome of the analytical (mathematical) model is compared with results obtained with the simulation tool ComFlo (Gerrits and Veldman 2003, Kleefsman *et al* 2005, Luppes *et al* 2005, 2006, Veldman *et al* 2007). Based on the Navier–Stokes equations for free-surface flows, this computational fluid dynamics (CFD) program can simulate the sloshing of two immiscible fluids with different densities and viscosities by means of finite-volume discretization techniques, including specially designed free-surface tracking algorithms.

In ComFlo, both liquids are simulated and tracked in time by solving the unsteady Navier–Stokes equations in conservative form for both fluids. In this so-called two-phase approach, incompressibility is assumed for both liquids, which is appropriate as they are indeed liquids, flowing at very low speed. As the flow inside the eggs under consideration is at very low speed, in combination with high viscosity and small scale (small eggs), the flow can be regarded as laminar and hence no turbulence modeling is required. The program uses an explicit time-stepping procedure to track the fluids in time. The maximum numerical time step is determined by
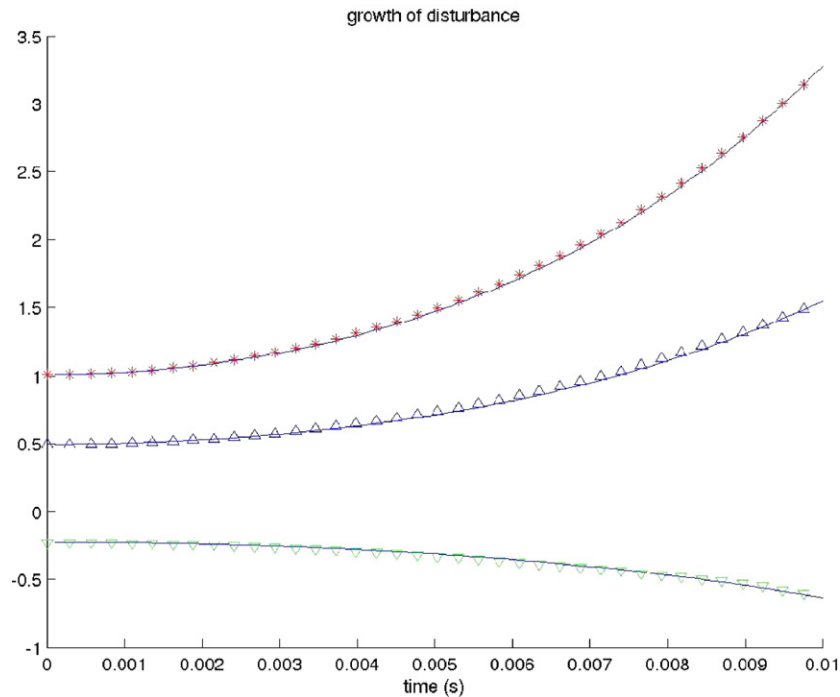
Figure 4. This figure shows ComFlo simulations (symbols) and hyperbolic cosine fit (solid lines) for, from top to bottom respectively, the coefficient of mode 01 in expansion of the interface in terms of the modes, and the heights of the highest and lowest points of the interface. These show that the growth of disturbances in the inverted system precisely follow a cosine hyperbolic form as predicted.

means of the well-known CFL number, which implies that the time step is limited by means of the combination of velocity magnitude and gridsize. The typical initial time step in the simulations described below is about 10 μs. However, since ComFlo is programmed to adjust the time step to an optimum value, during the simulation it normally goes to about 0.2 ms. Before we use ComFlo for testing the theory described above, we compute the dot product of each pair of the modes using the actual mesh size used in the ComFlo software. Since the software works with a Cartesian mesh this is calculated as

$$\langle f_{mn}(x, y), f_{m'n'}(x, y) \rangle$$
$$= \sum_i \sum_j f_{mn}(x_i, y_j) f_{m'n'}(x_i, y_j) \Delta x_i \Delta y_j. \quad (19)$$

This helps to quantify the magnitude of the numerical error we have for calculation of each dot product, and to check whether or not these modes are orthonormal, i.e. equation (19) should evaluate to zero for $(m, n) \neq (m', n')$, and unity for $(m, n) = (m', n')$. The numerical error in the dot products from zero for 125 000 (50×50×50) mesh points and $\varepsilon = 0.05a$ was around 0.5% of each one of the functions squared, indicating that the simulations on that mesh are sufficiently accurate. By increasing the number of meshpoints and hence decreasing the mesh size, grid independence can be confirmed, as two solutions on two grids only differ marginally.

In order to check the results of the theory and to see whether the modes we found are in fact the normal modes of the system, we use the criterion that if a linear system is excited with one of its normal modes it will vibrate with the same mode while the other normal modes remain unexcited. To check this, ComFlo simulations were started, each time

with one of the modes as an initial interface between the two fluids with the heavier fluid at the bottom. Then, after several steps, the coefficients of expansion of the new interface were calculated and monitored versus time. It was expected that the new interface only had a nonzero coefficient for the starting mode within the errors due to a finite mesh size. This starting coefficient would then undergo a damped oscillation around and toward zero. Some results of this kind are given in figure 5, which shows the plots of the coefficients of expansion versus time for some of the modes. This clearly shows that the modes we found in (8) are orthogonal and, in fact, to a very good approximation are the normal modes of our system. This is, theoretically, based on the completeness of the set of functions in (8) and the fact that we can write any integrable function over the domain $r \leqslant a$ as a linear combination of these functions (Greenberg 1998).

Using ComFlo simulations we also found the growth rate of each mode according to the formula

$$\alpha = \frac{1}{t} \cosh^{-1}\left(\frac{y}{y_0}\right) \quad (20)$$

where y_0 and y are the initial and final amplitudes of each mode when it increases for the time period t.

As mentioned above, the theoretical calculation of the effective mass involved in vibration of each mode is not easy to do. Instead, we can have an estimate for the ratio of mass involved in each oscillation by comparing the results of some analytical calculations with ComFlo experiments. If the total initial potential energy of the system is considered as the vibrational energy of the effective mass involved (m), as we can see from relations (17) or (18), the growth rate (α) and the period of oscillation (τ) are proportional to $m^{-1/2}$ and
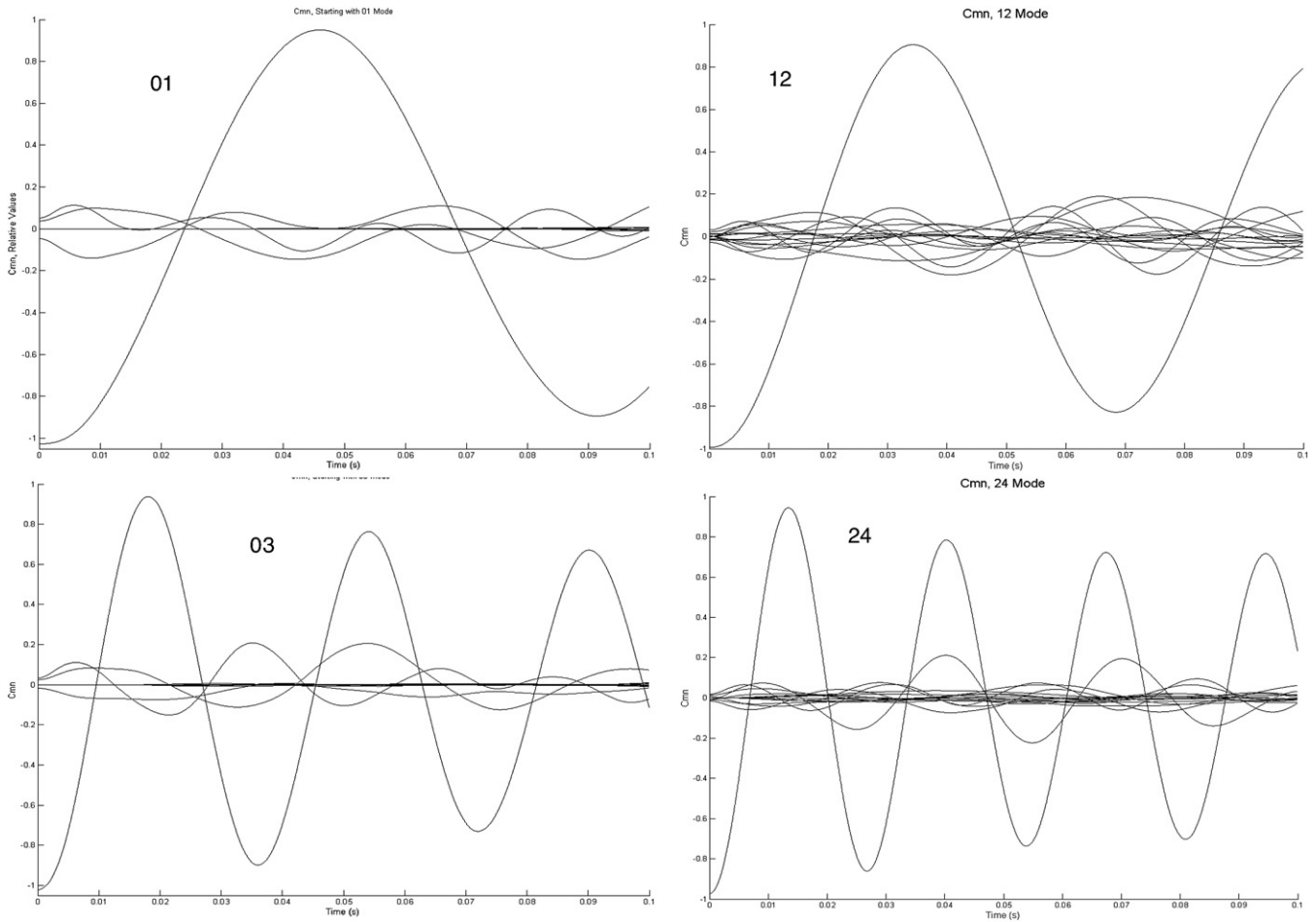
Figure 5. A few examples of oscillation of the modes. For each simulation, the system is started with the interfacial surface to be one of the modes with the heavy fluid at the bottom. Then at a later time the interfacial surface is expanded in terms of all the modes and the coefficient of each mode is calculated. Each plot shows these coefficients versus time, indicating that to a fairly good approximation, only the initial mode is oscillating and the rest of the modes stay calm, showing that the modes are in fact the normal modes of the system. The total time scale is 0.1 s; the vertical range is $[-1, 1]$ in arbitrary units for all plots showing their relative amplitude of oscillation. The numbers in the plots show the parameters (m and n) of the mode used as a starting shape in each case.

$m^{1/2}$, respectively. In the case of a vibration, the growth rate is imaginary and its magnitude represents the frequency of the oscillation. When the denser liquid is at the bottom, the maximum potential energy is positive and from the first part of relations (18) the negative sign under the square root accounts for the imaginary number.

Table 2 shows, in the second column, the values of the total potential energy in nano-Joules for each mode taken from the sum of the absolute values of the gravitational potential energy and the surface energy from table 1. The third column shows the value of the inverse square root of the second column, normalized to give the right value for mode 11. It is assumed that if the effective mass for all modes were the same, all other values would match as well and this would give the correct period for all modes. The difference between these is assumed to arise from the different effective mass involved in oscillation of the various modes. In fact, from relations (17) and (18) the ratio of the values of the two columns is the same as the ratio of the effective mass for that mode to that of mode 11 (or m_{eff}/m_{eff11}). Figure 6 shows the velocity fields in arbitrary

Table 2. The values of ΔU_{mn}^{tot} measured in nJ, $\sqrt{1/\Delta U_{mn}^{tot}}$ proportionally changed to match the *in silico* experiment for the mode 11, the experimental values of period of oscillation (τ) and estimated relative effective mass (m_{eff}) for the first few modes when water is at the bottom half.

| Mode	ΔU_{mn}^{tot} (nJ)	τ, theory (*s*)	τ, experiment (*s*)	$m_{eff}/m_{eff,11}$
01	130.6	0.104 15	0.0913	0.768
02	161.4	0.093 67	0.0611	0.425
03	208.5	0.082 42	0.0406	0.242
04	206.4	0.073 76	0.0320	0.188
11	55.89	0.159 20	0.1592	1.000
12	78.32	0.134 48	0.0723	0.289
13	102.0	0.117 84	0.0498	0.178
14	128.2	0.105 11	0.0366	0.121
21	44.35	0.178 73	0.1126	0.397
22	92.15	0.123 99	0.0612	0.244
23	121.6	0.107 91	0.0433	0.161
24	150.4	0.097 06	0.0326	0.113
31	43.77	0.179 91	0.0911	0.257
32	105.9	0.115 64	0.0528	0.209
33	140.1	0.100 55	0.0379	0.142
34	171.2	0.090 96	0.0287	0.100
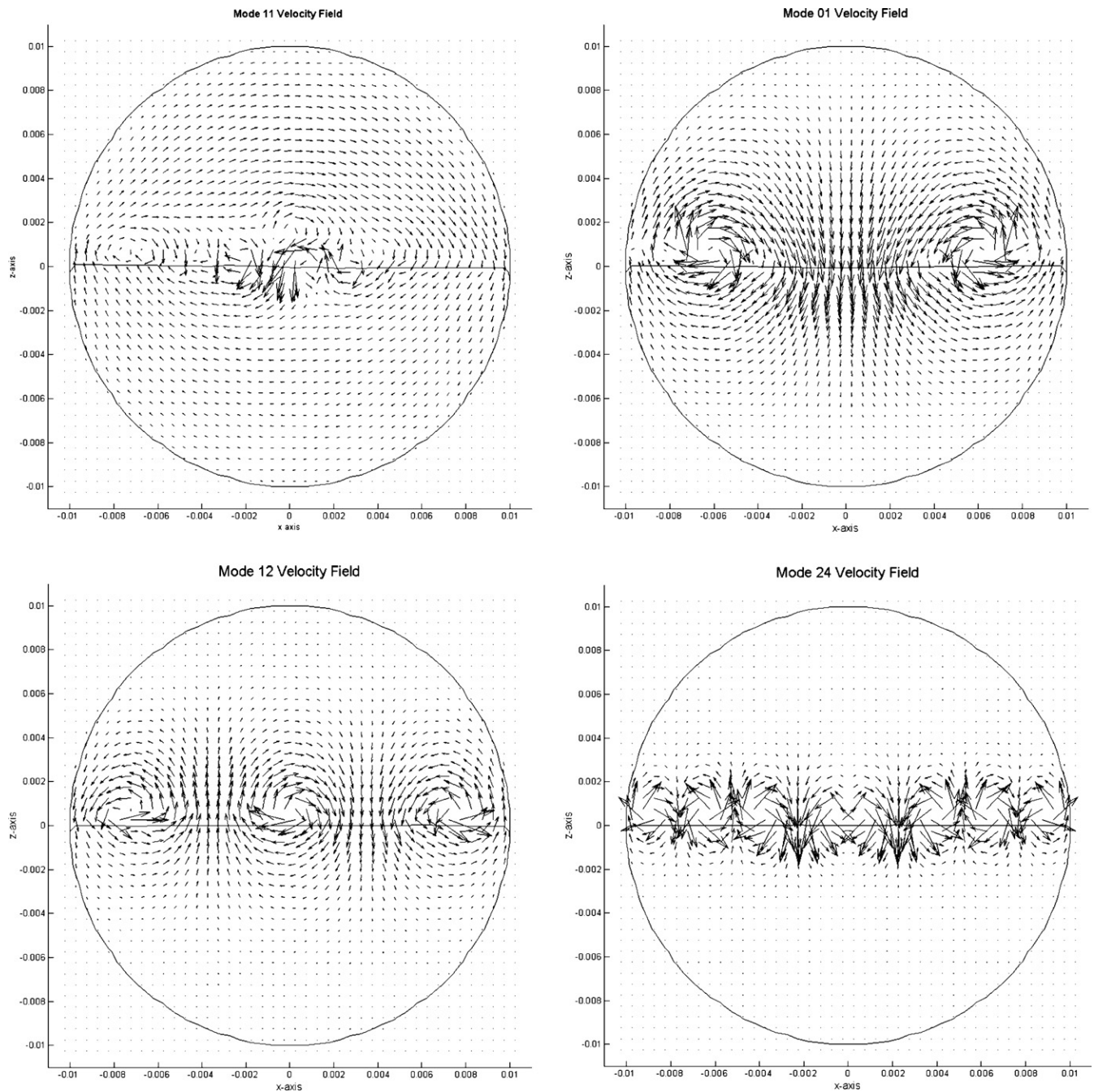
Figure 6. Velocity fields in arbitrary units in the middle vertical slice of the sphere with heavy fluid at the bottom. This figure shows that the numerical values estimated for the effective mass in table 2 are reasonable. The actual magnitude of the velocity of each volume element is not important here, but the rate at which their magnitude decays as we go away from the interfacial surface is important and indicates the amount of mass oscillating in each mode.

units in each volume element in the cross-section of the embryo for a few different modes taken from ComFlo simulations. The figure shows that the effective mass ratios we found in table 2 are reasonable. The important factor to be observed in these figures is the rate at which the velocity vectors decay as we go away from the interface of the two fluids, not the actual magnitude of the velocities. The figures also show that for mode 11, almost all the fluid mass is oscillating together but for the other modes only part of the mass is moving and therefore these modes have a smaller effective mass that actually undergoes oscillations. This should be taken

into consideration because the initial total potential energy is used for different amounts of oscillating (effective) mass for different modes, and this affects the predicted frequency or period of oscillation or the growth rate in the case of an inverted system.

Once we have the effective mass ratios we can use them to calculate the growth rates for each mode when the heavy liquid is on top. When the embryo is upside down, for each mode of oscillation and with the same amplitude (ε) the surface energy for the modes is the same but the gravitational potential energy will be negative. Therefore, the total potential energy change
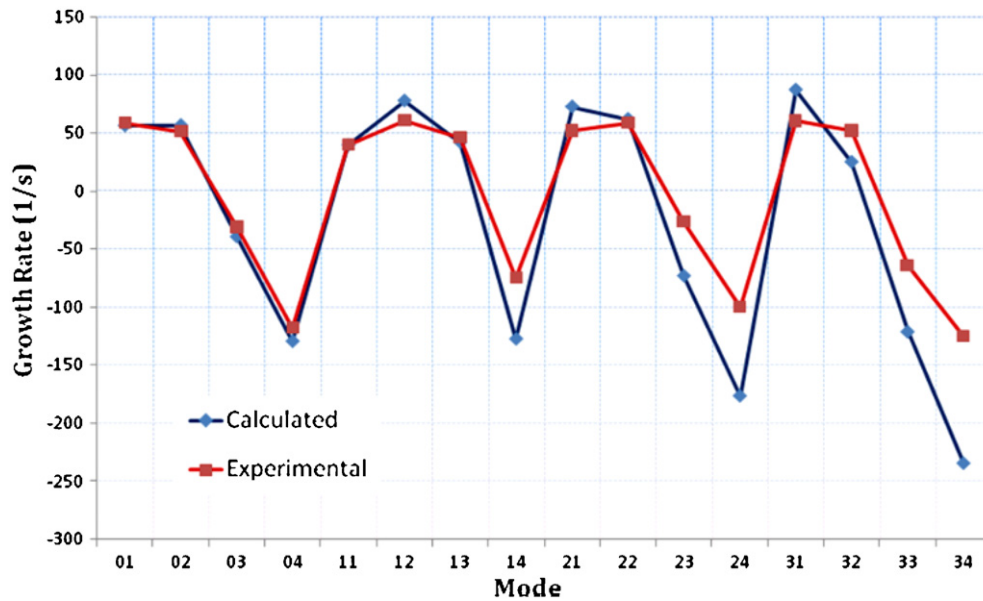
Figure 7. Comparison of the *in silico* experimental growth rates with calculated results. The negative growth rates correspond to the oscillating modes since the total potential energy for those modes is positive.

from the flat (equilibrium) configuration can be positive or negative depending on the mode. Those modes with positive total energy will oscillate around the equilibrium (for a short while until they decay), and the ones with negative potential energy grow with a hyperbolic cosine form with a growth rate estimated analytically as in (18) or experimentally as in (20). Changing viscosity of the fluids changes the rates of increase of the unstable modes and also damps the oscillation of stable modes but does not change the instability behavior of the modes. This means that changing viscosity of the liquid does not make an unstable mode stable and vice versa. This is the reason viscosity of the fluid is not playing a significant role in our discussions. It also means that this aspect of embryogenesis is robust with respect to changes in viscosity of yolk and cytoplasm, i.e., with respect to changes in temperature and/or nutrition.

Figure 7 compares the results of analytical estimation of growth rates for each mode with those calculated from ComFlo simulations for our model embryo. This shows a fairly good agreement between the two. In this figure, the growth rates of the stable modes are shown with a negative sign. In fact, mathematically, when a mode is oscillating around the equilibrium instead of growing, its growth rate becomes purely imaginary. Since plotting purely imaginary numbers along with positive real numbers is not convenient, we replaced the imaginary unit number (i) with a negative sign in this figure.

Up to this point we showed that the analytical calculations (with approximation of the wave equations we used from the beginning) agree with the computational fluid dynamic simulations (which take into account the exact Navier–Stokes equations for its calculations) for the study of Rayleigh instability of our model. In the following we try to apply this theory to an actual egg and try to get the probability of the survival of the eggs after inversion based on the calculations we carried out above.

Estimation of the probability of normal development of inverted embryos

Measurements of viscosity of cytoplasm range from as little as 430 to as much as 27 000 poise (Drury and Dembo 2001, Hochmuth and Needham 1990, Hochmuth *et al* 1993, Needham 1991, Tran-Son-Tay *et al* 1994, Valberg and Albertini 1985). Surprisingly intra-nuclear viscosity is at the lower end of this range, at 520 poise (Tseng *et al* 2004). Thus the large nucleus or 'germinal vesicle' of the one-cell axolotl embryo may not affect the general flow, except for the presence of the nuclear membrane. While we have ignored its role in the calculations here, the obvious buoyancy of the germinal vesicle relative to the yolk, on which it sits like a sessile drop, will have to be taken into account in future work. For example, it could, as a separate compartment, alter the mass of fluid available to be moved by different modes, though this would depend on the nuclear membrane bending modulus and tethering to cytoskeleton.

For surface tension we have available reported values such as 'a membrane cortical tension of 0.024 dyne cm^{-1}' (Tran-Son-Tay *et al* 1994) (cf Hochmuth *et al* (1993)). We have used the range of 20–80 dynes cm^{-1} for diatom raphe fluid found in the microcapillary, microfluidics channel that is part of their motility mechanism (Gordon and Drum 1970).

For these values of surface tension and the density contrast of about 40% between the yolk ($\rho_1 = 1.3$ g cm^{-3}) and cytoplasm ($\rho_2 = 0.9$ g cm^{-3}), the actual growth rates of different modes in the inverted system were calculated from ComFlo simulations. The density contrast is based on a guesstimate from our measurement of a mean density of $\rho = 1.1$ g cm^{-3}. The simulations were done starting from an amplitude of about 2% of the embryo radius of 1 mm for each mode and for the first 10 ms of the growth of the perturbation. Then the growth rates were calculated using equation (20).
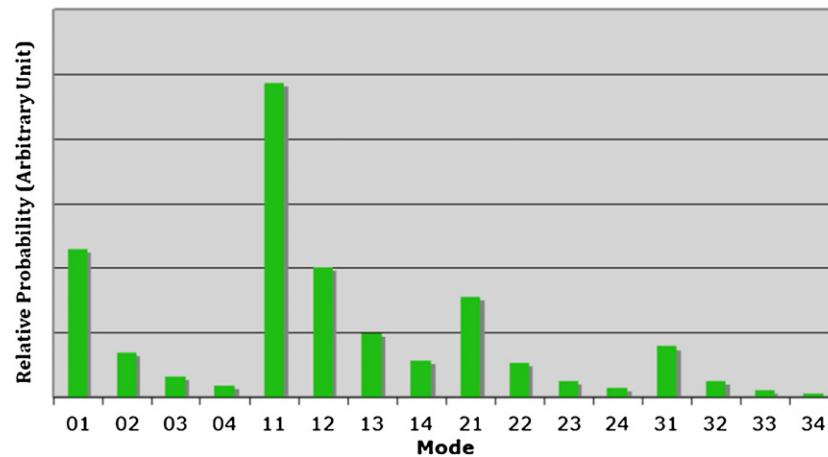
Figure 8. Estimated relative probability of growth of the modes, in arbitrary units, based on the ComFlo simulations with the surface tension and relative densities of the yolk and cytoplasm found in the literature.

The probability of each mode occurring at the beginning of an inversion is also estimated as proportional to $(mn)^{-2}$ for different modes except for the case of $m = 0$ for which a factor of $1/\pi$ is used. The results are plotted in figure 8, which shows the relative probability of growth of each mode of perturbation when an embryo is inverted, in arbitrary units for the 16 most important modes versus the corresponding mode numbers.

From the shape of the modes (figure 2) one can see that all the modes with $m = 1$ result in asymmetric sloshing of the yolk down the axis of the spherical embryo, while the growth of other modes ($m = 0$) turns into axisymmetric flow of the yolk. The former cause the cortical microtubules to align in one direction and therefore their effects are similar to that of a normal cortical rotation. The axisymmetric flow, on the other hand, prevents unidirectional pattern formation for microtubules and stops the normal development of the embryo as if the cortical rotation had not occurred. Therefore, in order to calculate the probability of survival of an embryo after an inversion we should calculate the total relative probability of the $m = 1$ cases to the total relative probability of the $m = 0$ cases. From the actual numbers used for the plot in figure 8 we can see that the rate of survival should be about 62% of the total.

Conclusion

Since the pioneering work of Wilhelm His (1888), there has been surprisingly little progress on the physics of embryos, especially above the molecular biology level (Beloussov and Gordon 2006, Chen and Brodland 2008, Forgacs and Newman 2005, Gordon 1983, 1994, Gordon and Jacobson 1978). The one-cell vertebrate embryo meets the physicist's general need for simplification, 'given a spherical cow . . .' (Harte 1988), for, indeed, a cow or a human or an axolotl is a sphere at this stage (Gordon 1999). Here we have shown that our empirical results using spherical flasks with two immiscible fluids (Flint *et al* 1989), which suggested that sloshing of the yolk in the one-cell amphibian embryo can account for its success or failure to develop when inverted, can indeed be justified

and made quantitative through analytical and computational fluid dynamics approaches. The next steps will be to predict the effects of these fluid motions on cortical microtubules that are believed to be responsible for cortical rotation and try to observe the yolk motion and alignment of the microtubules. Then we should be prepared to comment on the relationship of these motions to the so-called maternal determinants, deposits of RNA present in the embryo and believed to have effects on subsequent embryo development (Sindelka *et al* 2008). The same tools may allow us to understand why nearly normal development of amphibian embryos occurs in microgravity (Black *et al* 1996). We have seen that gravity is a subtle tool for probing embryos. Its effects extend to the molecular level (Portet *et al* 2003) and appear to affect subcellular organization of structures such as microtubules. Of course, the critical experiment to test the predictions made in this paper is to watch the three-dimensional flow pattern inside an inverted one-cell embryo, say by microMRI (Gruwel *et al* 2007a, 2007b) or microCT (Gordon and Del Bigio 2002), and see if it correlates one to one with whether or not the embryo subsequently develops. We hope that what we have done here is to begin a research program to understand the physics of the embryo and its interaction with its molecular and genetic components, toward building our understanding in the same order in which an embryo builds itself, starting from an initial state that is indeed relatively simple to comprehend.

Acknowledgments

References

Abramowitz M and Stegun I A 1965 *Handbook of Mathematical Functions* (New York: Dover)

Ancel P and Vintemberger P 1948 Recherches sur le déterminisme de la symétrie bilaterale dans l'oeuf des amphibiens/Research on the determinism of bilateral symmetry in the egg of the amphibian *Bull. Biol. Fr. Belg.* 31(Suppl.) 1–182

Beloussov L V and Gordon R 2006 Preface. Developmental morphodynamics: bridging the gap between the genome and embryo physics *Int. J. Developmental Biol.* **50** 79–80

Black S, Larkin K, Jacqmotte N, Wassersug R, Pronych S and Souza K 1996 Regulative development of *Xenopus laevis* in microgravity *Adv. Space Res.* **17** 209–17

Bordzilovskaya N P, Dettlaff T A, Duhon S T and Malacinski G M 1989 Developmental-stage series of axolotl embryos [Erratum: Staging Table 19–1 is for 20 °C, not 29 °C] *Developmental Biology of the Axolotl* ed J B Armstrong and G M Malacinski (New York: Oxford University Press) pp 201–19

Chang P, Pérez-Mongiovi D and Houliston E 1999 Organisation of *Xenopus* oocyte and egg cortices *Microsc. Res. Tech.* **44** 415–29

Chen X and Brodland G W 2008 Mechanics of amphibian neurulation elucidated using a multi-scale finite element model *Phys. Biol.* **5** 015003

Chung H M and Malacinski G M 1982 Pattern formation during early amphibian development: embryogenesis in inverted anuran and urodele eggs *Dev. Biol.* **93** 444–52

Chung H M and Malacinski G M 1983 Reversal of developmental competence in inverted amphibian eggs *J. Embryol. Exp. Morph.* **73** 207–20

de Gennes P-G, Brochard-Wyart F and Quéré D 2004 *Capillarity and Wetting Phenomena: Drops, Bubbles, Pearls, Waves* (New York: Springer)

Denegre J M and Danilchik M V 1993 Deep cytoplasmic rearrangements in axis-respecified *Xenopus* embryos *Dev. Biol.* **160** 157–64

Drury J L and Dembo M 2001 Aspiration of human neutrophils: effects of shear thinning and cortical dissipation *Biophys. J.* **81** 3166–77

Elinson R P and Holowacz T 1995 Specifying the dorsoanterior axis in frogs: 70 years since Spemann and Mangold *Curr. Top. Dev. Biol.* **30** 253–85

Elinson R P and Rowning B 1988 A transient array of parallel microtubules in frog eggs: potential tracks for a cytoplasmic rotation that specifies the dorso-ventral axis *Dev. Biol.* **128** 185–97

Flint R W, Gordon R, Martin C C and Brodland G W 1989 Simulation of the inversion of amphibian eggs in a gravitational field using hollow glass spheres *Microgravity as a Tool in Developmental Biology, Selected papers from a special ESA Symposium held during the 11th International Congress of the International Society of Developmental Biologists, (Utrecht, 20–25 August 1989)* ed G A Ubbels, H Oser and T D Guyenne (Paris, Cedex: European Space Agency) pp 81–3

Forgacs G and Newman S A 2005 *Biological Physics of the Developing Embryo* (Cambridge: Cambridge University Press)

Gerhart J C, Danilchik M, Doniach T, Roberts S, Rowning B and Stewart R 1989 Cortical rotation of the *Xenopus* egg: consequences for the anteroposterior pattern of embryonic dorsal development *Development* 107 (Suppl.) 37–51

Gerrits J and Veldman A E P 2003 Dynamics of liquid-filled spacecraft *J. Eng. Math.* **45** 21–38

Gordon R 1983 Computational embryology of the vertebrate nervous system *Computing in Biological Science* ed M Geisow and A Barrett (Amsterdam: Elsevier/North-Holland) pp 23–70

Gordon R 1994 Mechanical engineering of the cytoskeleton in developmental biology [Editor] *Int. Rev. Cytol.* **150** 1–431

Gordon R 1999 The Hierarchical Genome and Differentiation Waves: Novel Unification of Development, Genetics and Evolution (Singapore and London: World Scientific and Imperial College Press)

Gordon R, Bohun C S, Breward C, Cumberbatch E, Djoumna G, ElSheikh A, Williams J F and Wylie J 2006 Yolk dynamics in amphibian embryos *Proc., Fields-MITACS Industrial Problem-Solving Workshop (FMIPW) (14–18 August 2006)* (Toronto: Fields Institute) pp 33–49

Gordon R and Del Bigio M R 2002 Time-lapse x-ray microscopy of early axolotl embryo development, *Proposal Submission to the Canadian Light Source Facilities Advisory Committee: Development of a BioMedical Imaging Beamline at the Canadian Light Source. Submitted 25 January 2002* ed C Christensen, D Quinn, E Kendall, B Juurlink, G Adams, K Tanino, G Fallone and I Cunningham (Saskatoon: The BioMedical Imaging Beamline Group) p 65

Gordon R and Drum R W 1970 A capillarity mechanism for diatom gliding locomotion *Proc. Natl Acad. Sci. USA* **67** 338–44

Gordon R, Goel N S, Steinberg M S and Wiseman L L 1972 A rheological mechanism sufficient to explain the kinetics of cell sorting *J. Theor. Biol.* **37** 43–73

Gordon R, Goel N S, Steinberg M S and Wiseman L L 1975 A rheological mechanism sufficient to explain the kinetics of cell sorting *Mathematical Models for Cell Rearrangement* ed G D Mostow (New Haven: Yale University Press) pp 196–230

Gordon R and Jacobson A G 1978 The shaping of tissues in embryos *Sci. Am.* **238** 106–13

Greenberg M D 1998 *Advanced Engineering Mathematics* 2nd edn (Upper Saddle River, NJ: Prentice-Hall)

Gruwel M L H, Lerner B, Crawford-Young S and Gordon R 2007a Early development of axolotl (*Ambystoma mexicanum*) embryos using MRI micro-imaging *Manitoba Institute of Child Health 3rd Annual Research Day (11 October 2007)* (Winnipeg: Manitoba Institute of Child Health)

Gruwel M L H, Lerner B, Crawford-Young S and Gordon R 2007b MR micro imaging of hard and soft materials *4th KrakówWinnipeg Workshop on Imaging Technology (Krakow, Poland, 2–5 October 2007)* (Kraków, Poland: Polish Academy of Arts and Sciences)

Harte J 1988 *Consider a Spherical Cow, A Course in Environmental Problem Solving* (Mill Valley, CA: University Science Books)

His W 1888 On the principles of animal morphology *R. Soc. Edinburgh Proc.* **15** 287–98

Hochmuth R M and Needham D 1990 The viscosity of neutrophils and their transit times through small pores *Biorheology* **27** 817–28

Hochmuth R M, Ting-Beall H P, Beaty B B, Needham D and Tran-Son-Tay R 1993 Viscosity of passive human neutrophils undergoing small deformations *Biophys. J.* **64** 1596–601

Kane J W and Sternheim M M 1983 *Physics* 2nd edn (New York: Wiley)

Kirschner M W, Gerhart J C, Hara K and Ubbels G A 1980 Initiation of the cell cycle and establishment of bilateral symmetry in *Xenopus* eggs *The Cell Surface: Mediator of Developmental Processes* ed S Subtelny and N K Wessells (New York: Academic) pp 187–215

Kleefsman K M T, Fekken G, Veldman A E P, Iwanowski B and Buchner B 2005 A volume-of-fluid based simulation method for wave impact problems *J. Comput. Phys.* **206** 363–93

Luppes R, Helder J A and Veldman A E P 2005 Liquid sloshing in microgravity *Proc. 56th Int. Astronautical Congress (Fukuoka, Japan)* paper IAC-05-A2.2.07, 11 pp

Luppes R, Helder J A and Veldman A E P 2006 The numerical simulation of liquid sloshing in microgravity *Proc. Eur. Conf. Computational Fluid Dynamics: ECCOMAS CFD 06 (Egmond aan Zee, The Netherlands)* ed P Wesseling, E Oñate and J Périaux (Delft: Technical University) paper 490, 19 pp

Malacinski G M and Neff A W 1989 The amphibian egg as a model system for analyzing gravity effects *Adv. Space Res.* **9** 169–76

Needham D 1991 Possible role of cell cycle-dependent morphology, geometry, and mechanical properties in tumor cell metastasis *Cell Biophys.* **18** 99–121

Neff A W and Malacinski G M 1982 Reversal of early pattern formation in inverted amphibian eggs *Physiologist* 25 (6 Suppl.) S119–S120

Neff A W, Smith R C and Malacinski G M 1986 Amphibian egg cytoplasm response to altered G-forces and gravity orientation *Adv. Space Res.* **6** 21–8

Neff A W, Wakahara M, Jurand A and Malacinski G M 1984 Experimental analyses of cytoplasmic rearrangements which follow fertilization and accompany symmetrization of inverted *Xenopus* eggs *J. Embryol. Exp. Morph.* **80** 197–224

Neff A W, Wakahara M and Malacinski G M 1990 Bifurcation of the amphibian embryo's axis: analysis of variation in response to egg centrifugation *Int. J. Dev. Biol.* **34** 391–8

Phillips C R, Whalon B, Moore J and Danilchik M 1996 Gravitational effects on the rearrangement of cytoplasmic components during axial formation in amphibian development *Adv. Space Res.* **17** 225–35

Portet S, Tuszynski J A, Dixon J M and Sataric M V 2003 Models of spatial and orientational self-organization of microtubules under the influence of gravitational fields *Phys. Rev.* E **68** 021903

Rayleigh L 1879a On the capillary phenomena of jets *Proc. R. Soc.* **29** 71–97

Rayleigh L 1879b On the instability of jets *Proc. London Math. Soc.* **10** 4–13

Rayleigh L 1892 On the instability of a cylinder of viscous liquid under capillary force *Phil. Mag.* **34** 145–54

Rayleigh L 1964 *Scientific Papers by Lord Rayleigh (John William Strutt)* (New York: Dover)

Rowlinson J S and Widom B 1982 *Molecular Theory of Capillarity* (Oxford: Clarendon)

Sindelka R, Jonák J, Hands R, Bustin S A and Kubista M 2008 Intracellular expression profiles measured by real-time PCR tomography in the *Xenopus laevis* oocyte *Nucleic Acids Res.* **36** 387–92

Tran-Son-Tay R, Kirk 3rd T F, Zhelev D V and Hochmuth R M 1994 Numerical simulation of the flow of highly viscous drops down a tapered tube *J. Biomech. Eng.* **116** 172–7

Tseng Y, Lee J S, Kole T P, Jiang I and Wirtz D 2004 Micro-organization and visco-elasticity of the interphase nucleus revealed by particle nanotracking *J. Cell Sci.* **117** 2159–67

Valberg P A and Albertini D F 1985 Cytoplasmic motions, rheology, and structure probed by a novel magnetic particle method *J. Cell. Biol.* **101** 130–40

Veldman A E P, Gerrits J, Luppes R, Helder J A and Vreeburg J P B 2007 The numerical simulation of liquid sloshing on board spacecraft *J. Comput. Phys.* **224** 82–99

Wakahara M, Neff A W and Malacinski G M 1984 Topology of the germ plasm and development of primordial germ cells in inverted amphibian eggs *Differentiation* **26** 203–10

Wakahara M, Neff A W and Malacinski G M 1985 Development of delayed gastrulae and permanent blastulae from inverted *Xenopus laevis* eggs *Acta Embryol. Morph. Exp.* **6** 193–209